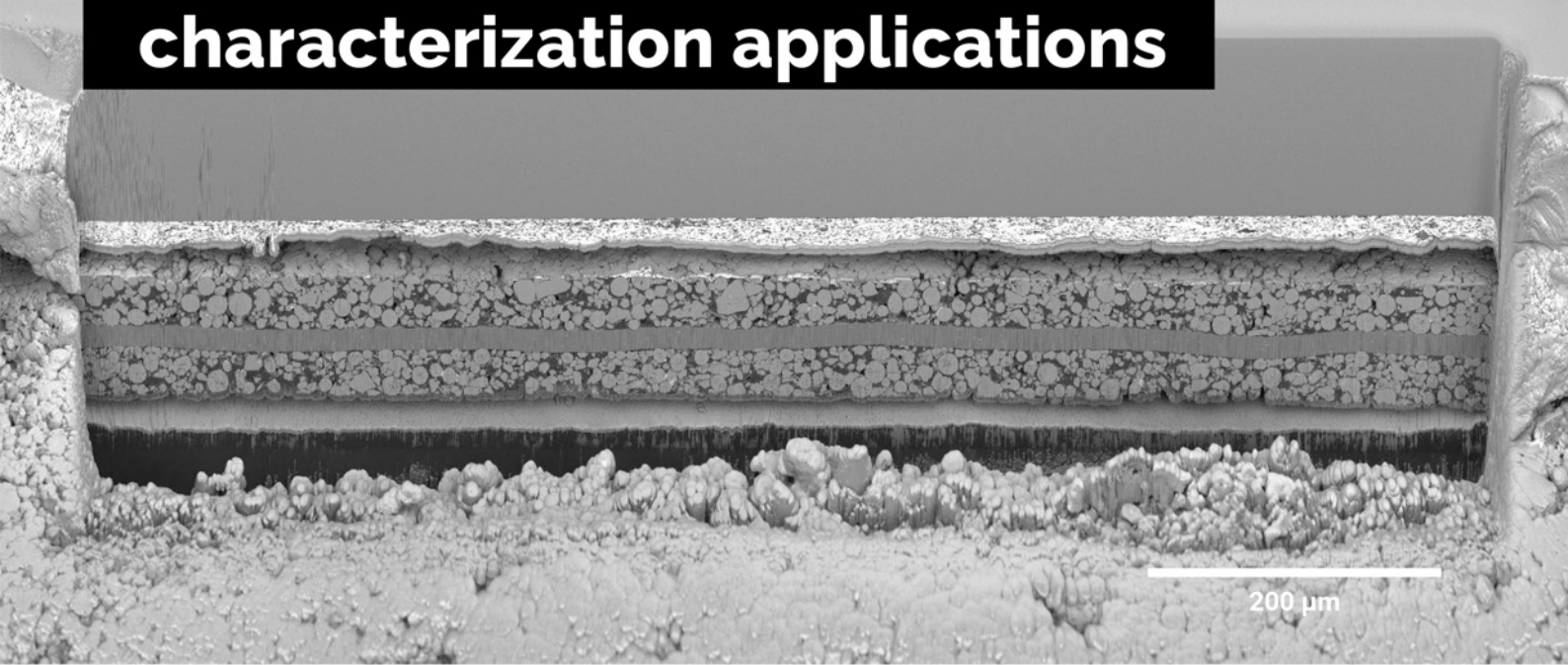


A unique combination of Plasma FIB and field-free UHR SEM for the widest range of multiscale materials characterization applications



1 mm cross-section through a Li-ion battery electrode

TESCAN AMBER X

- ✓ High throughput, large area FIB milling up to 1 mm
- ✓ Ga-free microsample preparation
- ✓ Ultra-high resolution, field-free FE-SEM imaging and analysis
- ✓ In-column SE and BSE detection
- ✓ Spot optimization for high-throughput, multi-modal FIB-SEM tomography
- ✓ Superior field of view for easy navigation
- ✓ Essence™ easy-to-use, modular graphical user interface



For more information visit

www.tescan.com

Machine-Learning-Based Exploration of Bending Flexoelectricity in Novel 2D Van der Waals Bilayers

Brahmanandam Javvaji, Xiaoying Zhuang,* Timon Rabczuk, and Bohayra Mortazavi

Accurate examination of electricity generation stemming from higher-order deformation (flexoelectricity) in 2D layered materials is a highly challenging task to be investigated with either conventional computational or experimental tools. To address this challenge herein an innovative and computationally efficient approach on the basis of density functional theory (DFT) and machine-learning interatomic potentials (MLIPs) with incorporated long-range interactions to accurately investigate the flexoelectric energy conversion in 2D van der Waals (vdW) bilayers is proposed. In this approach, short-range interactions are accurately defined using the moment tensor potentials trained over computationally inexpensive DFT-based datasets. The long-range electrostatic (charge and dipole) and vdW interaction parameters are calibrated from DFT simulations. Elaborated comparison of mechanical and piezoelectric properties extracted from the herein proposed approach with available data confirms the accuracy of the devised computational strategy. It is shown that the bilayer transition metal dichalcogenides can show a flexoelectric coefficient 2–7 times larger than their monolayer counterparts. Noticeably, this enhancement reaches up to 20 times for Janus diamane and fluorinated boron-nitrogen derivatives of diamane bilayers. The presented results improve the understanding of the flexoelectric effect in vdW heterostructures and moreover the proposed MLIP-based methodology offers a robust tool to improve the design of novel energy harvesting devices.

1. Introduction


Flexoelectricity is the emerging electromagnetic coupling type that generates electricity under mechanical deformations and vice versa. Solid perovskite materials well studied to avail this electricity.^[1–4] However, recent research interest has turned to 2D materials due to their highly promising features, like achieving larger strain gradients, a wide choice of materials (also bio-compatible), and miniature and effective energy conversion rate. Applications involving flexoelectricity are not only limited to energy harvesting^[5,6] but also bone crack-healing,^[7] memory reading,^[8] memory writing,^[9] sensors,^[10] silicon Schottky diodes.^[11] On the other hand, a vast development of 2D van der Waals (vdW) materials is highly aspiring. Especially, the material property dependency with the number of layers, translational and rotational stack sequencing, and ability to stack different materials due to weak vdW forces shade light into new research directions and raise open questions. Deeply investigated the fundamental electronic, mechanical, and thermal properties of vdW layers. Review

articles^[12–14] focus on the current state of research and the devices using the vdW layers. The inter-layer electronic interactions^[15] transfer the charges among the layers and help to generate polarization. Layered GdTe₃ material exhibit exceptional electron mobility than its bulk counterpart.^[16] The flexoelectricity coupled with photoelectric effect enhances the separation of electron–hole pairs in bent 2D semiconductors.^[17] The vertical piezoelectricity (electricity due to mechanical strain) for Janus multilayer transition metal dichalcogenides (TMDs)^[18] is higher than the conventional quartz crystal. Using two Janus TMD monolayers, a tribo-piezoelectric nano energy generator with high power densities is predicted.^[19] The symmetry breaking in twisted bilayer graphene induces flexoelectric polarization.^[20] In a double layer MoS₂ nanotubes, curvature induced voltage generation is estimated.^[21]

The experimental investigation on flexoelectric coefficients uses piezoresponse force microscopy (PFM)^[22,23] for monolayers of TMDs. Other studies also use PFM for thin (more than 2 nm) LaAlO₃^[24] and MoS₂^[25] to predict the flexoelectricity. In order to minimize the experimental burdens, expert investigation on fine-scale physics and faster exploration across different materials, numerical models are assuredly helpful. Theoretical studies on carbon nanoshells provide electronic rehybridization due to

B. Javvaji, X. Zhuang, B. Mortazavi
Institute of Photonics
Faculty of Mathematics and Physics
Cluster of Excellence PhoenixD (Photonics, Optics, and
Engineering–Innovation Across Disciplines)
Gottfried Wilhelm Leibniz Universität Hannover
30169 Hannover, Germany
E-mail: zhuang@iop.uni-hannover.de

X. Zhuang, T. Rabczuk
College of Civil Engineering
Tongji University
1239 Siping Road, Shanghai 200092, China
T. Rabczuk
Institute of Structural Mechanics
Bauhaus Universität Weimar
Marienstr. 15, 99423 Weimar, Germany

 The ORCID identification number(s) for the author(s) of this article can be found under <https://doi.org/10.1002/aenm.202201370>.

© 2022 The Authors. Advanced Energy Materials published by Wiley-VCH GmbH. This is an open access article under the terms of the Creative Commons Attribution License, which permits use, distribution and reproduction in any medium, provided the original work is properly cited.

DOI: 10.1002/aenm.202201370

curvature,^[26] which create a dipole moment. A recent density functional theory (DFT) study explores the flexoelectric property in many 2D materials by considering the changes in radial polarization,^[27] and another one uses a potential difference across the nanotube cross-section.^[28] Those studies differ in terms of the flexoelectric coefficients due to the involvement of different contributions for total polarization. To estimate flexoelectricity, the periodic ripple patterns are introduced in a 2D sheet.^[29,30] Explored the flexoelectric dipole moment in nanocones and nanotubes using DFT.^[31,32] In regard of flexoelectricity in vdW layers, issues like vertical non-periodicity, different stacking possibilities, grain boundaries, Moiré patterns, computational costs, and mainly creating a bent configuration are unable to handle with the DFT simulations alone. The present work focuses on handling these issues in molecular dynamics (MD) environment by deriving the accurate interatomic potentials from first-principle simulations.

In doing so, we consider three materials groups, TMDs, diamanes and BNdiamanes. We propose the BNdiamanes by replacing the carbons in the native diamane structure with alternate boron and nitrogen atoms. Monolayer diamane exhibited improved flexoelectric response compared to conventional TMD monolayer^[33] thus, the boron–nitrogen bonds create extra asymmetry in BNdiamane and may help in flexoelectric effect. Figure S1, Supporting Information, shows the stacking configurations considered in the present work for these material groups. The dashed line indicate the atomic alignment in both the layers. To utilize the MD framework, the availability of accurate interatomic potential is essential. Recent machine learning based moment tensor potential (MTP) parameters provide high accuracy in predicting the mechanical and thermal properties for monolayer 2D materials. This study employs MTP for short-range interactions and derives the long-range interaction parameters from DFT simulations. To induce a natural bending response to the vdW layers the present work proposes compressing only the edges of 2D material and analyzing the resulting configuration. Such models are extremely impracticable through DFT simulations due to the limitation of periodic boundary condition. The proposed deformation process is highly and effectively possible with the derived inter-atomic potentials in MD environment. The performed simulations in the manuscript are divided into three parts: 1) Generating the inter-atomic potential parameters:- First we prepare the data sets at high and low temperatures for the considered vdW bilayers and obtain MTP parameters through the machine-learning interatomic potentials (MLIPs) scheme. Lennard-Jones (LJ) and charge-dipole (CD) potential parameters are obtained next by matching the DFT measured inter-layer energy and polarizability with the MD simulations. 2) Validating the potential parameters:- The initial tests are assigned to validate the potential parameters by comparing the mechanical and piezoelectric properties with available data in the literature and through standalone DFT simulations. 3) Bending under compression:- The compression simulations are performed for the bilayer systems with the developed potential parameters and then extracted the flexoelectric coefficients by processing the generated atomic data.

2. Results and Discussion

The atomic interactions in bilayer systems are divided into short-range and long-range contributions. **Figure 1a** illustrates

the schematic of layer separation and consideration of neighbor atoms restricted to each layer separately. We perform ab initio molecular dynamics (AIMD) simulations over bilayer supercells with 1 nm² area at 50 and 600 K temperature, each for 1000 time steps. Out of these steps, half of the full trajectories were selected to create the training sets, which consist of positions \mathbf{r} , energy e , forces \mathbf{f} , and stress σ as input for passive fitting implemented in the machine learning inter-atomic potential package.^[34] The methodology for efficient training of MTPs are explained in early works.^[35–37] To derive the long-range vdW inter-layer interaction parameters, we modify the unitcell size in z -direction as 50 Å for the optimized bilayer unitcell. This helps to avoid the unnecessary interaction/contributions from the periodic replicas along the z -direction. We set this limit to be about five times larger than the maximum distance of separation between the two layers in a bilayer system (as seen in Figure S2, Supporting Information). Next, we vary the inter-layer distance h between the two monolayers in a bilayer unitcell and perform electronic self-consistent calculations taking into account the vdW dispersion correction using the DFT-D3 method of Grimme.^[38,39] We record the total energy of the bilayer system as a function of inter-layer distance. The inter-layer energy from DFT simulations (ϕ_{DFT}) is the difference of energy from bilayer unitcell and twice the monolayer energy. We now perform classical single step MD simulation with no velocity involvement for a simulation cell area 4 nm² with in-plane (x and y) periodic boundary conditions. The generated MTP parameters and LJ parameters (ϵ and ψ) define the pair interaction potential. The inter-layer energy from MD (ϕ) simulations is defined as the energetic interaction across the atomic layers. Figure 1b indicates the neighbor atom selection. Atom belongs to the bottom layer has a set of neighbors from the top layer. The LJ parameters for each atom type in a bilayer unitcell are determined by establishing a close match between ϕ and ϕ_{DFT} . Figure 1b and Figure S2, Supporting Information, depicts the comparison between ϕ and ϕ_{DFT} . The atomic positions in optimized bilayer unitcell were updated with the minimum energetic distance of separation (h_0). The CD model was added to the short-range MTP and LJ potentials to estimate the deformation-induced electrical polarization. According to CD model, each atom carries a charge q and dipole moment \mathbf{p} . This model is dependent on the parameter R for each atom type, which is related to total polarizability. We adjust R to match the atomic polarizability estimated from DFT α_{DFT} (using GAUSSIAN software^[40]) to the calculated polarizability from CD model α (schematic shown in Figure 1c). The early works from authors cover the calculation of CD parameters and implementation of CD model in MD environment.^[41,42]

The initial tests aim to benchmark the derived potential parameters. The in-plane elastic modulus (E^I) under tensile stretching deformation estimated from the slope of stress σ_{yy} to strain ϵ_{yy} (upto 1%). **Figure 2a** shows the elastic modulus for bilayer systems with stacking order a, which are in excellent agreement with the DFT predicted elastic modulus E^I_{DFT} . The elastic modulus for bilayer SeMoS, HCF, and HBNF are 221, 917, and 699 N m⁻¹, respectively. The corresponding monolayer values were calculated as 109, 460, and 332 N m⁻¹. This fulfills the expected twice increment of elastic modulus due to the involvement of two monolayers. Note that, we avoided

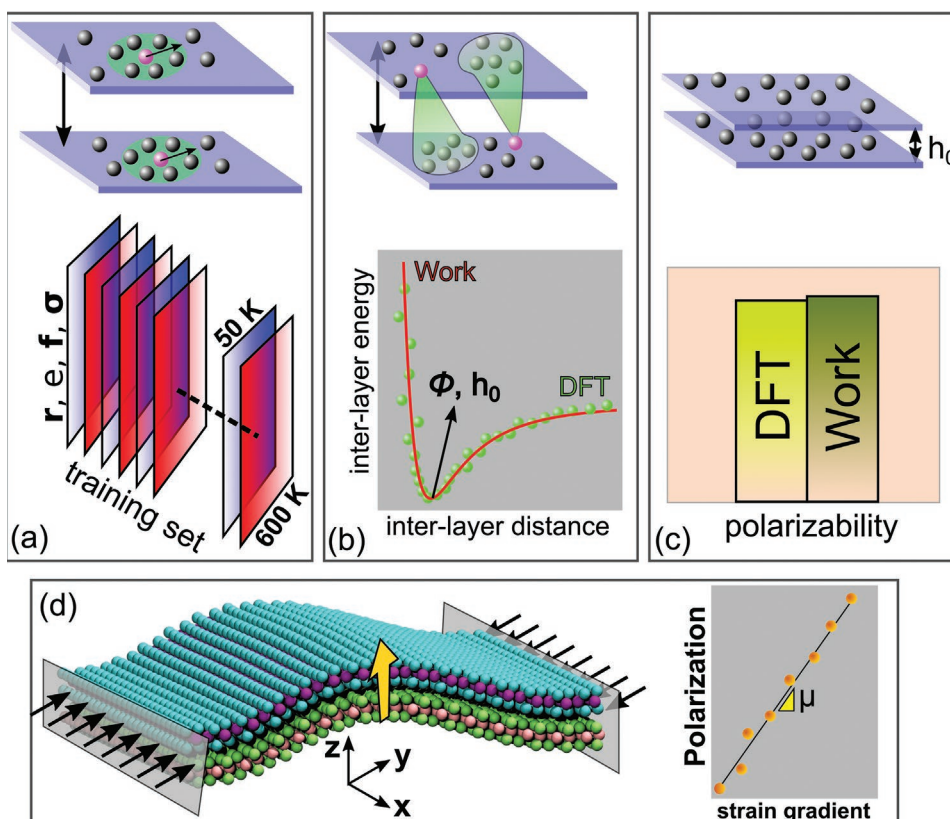


Figure 1. a) Schematic bilayer configuration with neighbor atom selection for short-range interactions. The vertical blue and red colored planes indicate the data ($\mathbf{r}, \mathbf{e}, \mathbf{f}$, and $\boldsymbol{\sigma}$) for training collected from atomic trajectories at 50 and 600 K temperatures. b) Highlighting the neighbor atom selection that accounting the vdW interactions in a bilayer configuration. The comparison between calculated (work) and DFT predicted inter-layer energy ϕ and inter-layer distance h . Arrow indicates the minimum energetic distance of separation h_0 and associated inter-layer energy ϕ . c) Illustrating the bilayer configuration with minimum energetic separation used to calculate the atomic polarizability. Establishing the matching between the polarizability from CD model (work) and from DFT calculations to predict the CD model parameter R that accounting the long-range charge-dipole interactions. d) Schematic of bending deformation under compression loading. The yellow colored arrow indicates the generated polarization due to flexoelectric effect. The expected linear response of polarization to strain gradient and the slope indicates the flexoelectric coefficient (μ).

using the thickness in the calculation of stress and polarization. Because of this, the reported Young's modulus is double for bilayer as compared with the monolayer counterpart. The inter-layer vdW interaction energy ϕ estimated for the given configuration is in match with the DFT predictions ϕ_{DFT} (see Figure 2a and values belong to right-hand side vertical axis). We also observe that ϕ is closely related to the earlier DFT predictions (ϕ_{REF} as open markers in Figure 2a) for bilayer SMoS ,^[43] SMoSe ,^[44] and SeMoSe ^[43] systems. This shows that the derived LJ parameters accurately capturing the inter-layer interactions. Diamane (TMD) bilayers have weak (strong) inter-layer energy. This trend is reversed in the case of elastic modulus. Figure 2b shows the high consistency exists between polarizabilities α and α_{DFT} . The bilayer α for SMoS is 39.33 \AA^3 which is 3.184 times higher than the monolayer α .^[45] The associated CD parameter R values increased by 1.27 times for the chalcogen (sulfur and selenium) atoms in bilayer SMoSe . In bilayer HCF, α rises only about 1.315 times that of monolayer HCF.^[33] The bilayer HBNF shows a rise of α nearly 1.9 times than the monolayer HBNF. The MD simulations were performed at a temperature of 1 K and DFT results acquired at ground state (0 K). Table S1, Supporting Information, indicates

the derived LJ and CD parameters for bilayer materials with stacking order a. Tables S2–S4, Supporting Information, provide several physical quantities (lattice constant, inter-layer energy, inter-layer distance, polarizability, and elastic modulus) for the bilayer stacking orders along with DFT values. Note that for diamanes, the parameter derivation executed only for Janus structure HCF-a. Using that, simulations for all other stacked configurations (b, c, d, and e) performed. Also, used the same parameters for the HCH and FCF bilayer systems. For BNdiamanes, the potential parameters derived for Janus HBNF and non-Janus HBNH and FBNF bilayers. This is due to the missing bond information from Janus HBNF alone. For example, the parameters for HCF used to perform HCH or FCF simulations. Since the required interactions (C–H and C–F) are known from HCF itself. In case of HBNF, interactions N–H and B–F are missing when using it for HBNH and FBNF, respectively.

Figure 2c shows the piezoelectric coefficients under in-plane and out-of-plane uniaxial stretching deformations for bilayer materials with stacking orders from a to e. From the slope of the total polarization P_y to the applied strain ϵ_{yy} , the piezoelectric coefficient e_{yyy} for SeMoS-d and SeMoS-e are noted

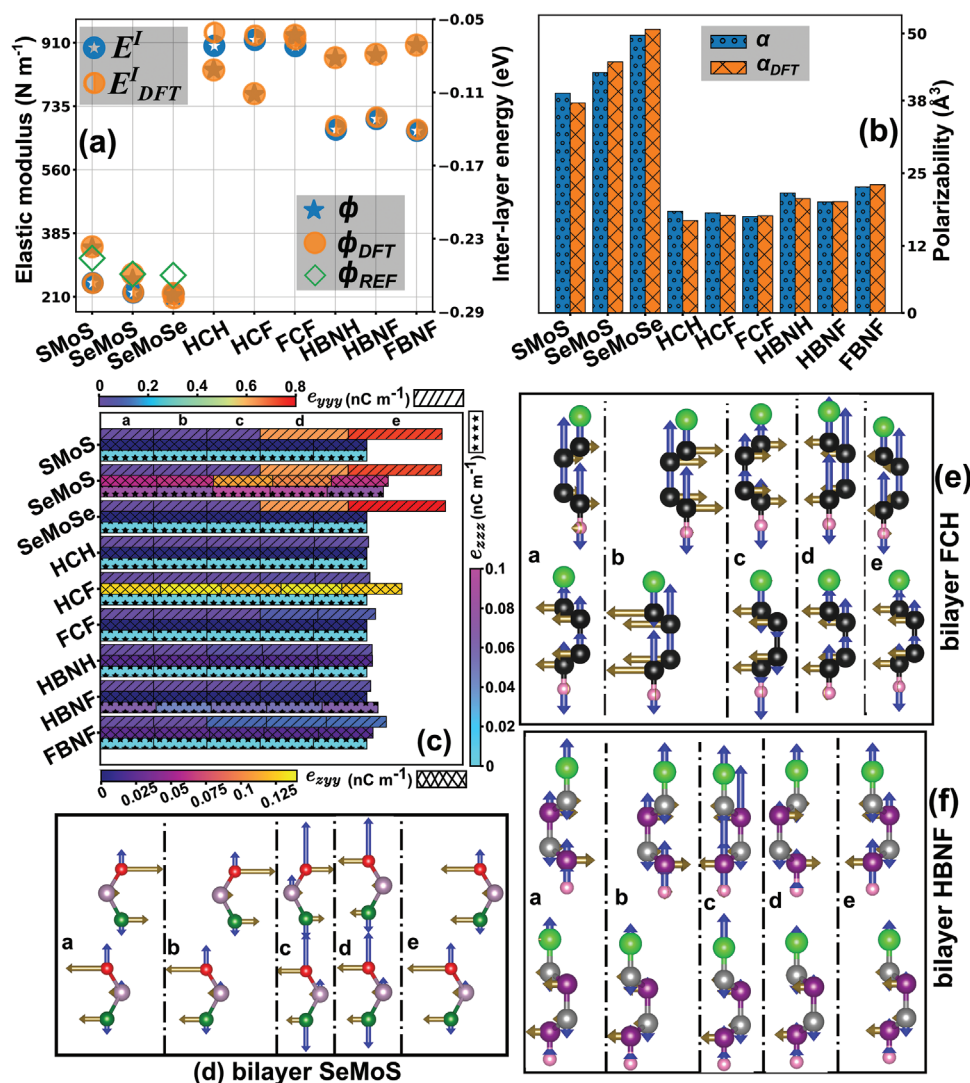


Figure 2. Comparison of a) elastic modulus, inter-layer energy and b) polarizability for various bilayer systems with same stacking computed using present modeling and using DFT calculations. c) Piezoelectric coefficients under in-plane and out-of-plane stretching deformation for various bilayer systems with a–e stacking. Bilayer d) SeMoS, e) FCH, and f) HBNF unitcells with different stacking representing the in-plane P_y and out-of-plane P_z polarization in arrows.

as 0.65 and 0.748 nC m⁻¹, which is nearly twice that of a monolayer SeMoS.^[18,45] Throughout the paper, the total polarization is the net dipole moment to the total area of the system. The 2D layer thickness is not utilized in defining the polarization. The stacking orders a–c are non-piezoelectric. The horizontal arrows in Figure 2d shows P_y is opposite in both the layers for a, b, and c stacking orders. This cancels the total polarization. In stacking order d and e, direction of P_y is aligned in both layers and results e_{zyy} as non-zero. Similarly in non-Janus SMOs and SeMoSe bilayers, a to c stacking orders show e_{zyy} as zero. For d, e stacking orders e_{zyy} is twice that of monolayers. The e_{zyy} for bilayer diamanes and BNdiamanes are an order smaller than TMDs, similar to the earlier reports on monolayers.^[33] The direction of polarization P_y is same as in TMDs (see Figure 2d,e).

In the out-of-plane direction, polarization P_z arises due to the Janus structure of each layer in SeMoS and HCF bilayers. Irrespective to the stacking order, P_z shows a linear change

with strain ϵ_{yy} which leads non-zero e_{zyy} piezoelectric coefficient. The sulfur atoms acquire higher polarization P_z than selenium atoms due to the high electron affinity of sulfur. For stacking orders, c and d noticed an enhanced P_z , which makes e_{zyy} as 1.72 times larger than SeMoS-a, SeMoS-b, and SeMoS-e. The e_{zyy} value for SeMoS-a is 0.061 nC m⁻¹, and for multilayer SeMoS is 0.047 nC m⁻¹.^[18] This confirms that the derived interatomic potentials accurately predict the electromechanical properties of bilayers. Note that the present results are specifically for bilayers without assuming periodicity in out-of-plane direction, whereas DFT predictions use the periodicity assumption. The non-Janus diamanes (HCH and FCF) do not yield P_z , and the e_{zyy} is zero. HCF-a to HCF-e bilayers yield e_{zyy} about two times higher than Janus TMDs. When compared with monolayer HCF, e_{zyy} is four times higher in bilayer HCF. The collective support from all the carbon atom dipole moments makes the polarization P_z high (see Figure 2e). There is a cancellation

of the dipole moment due to the boron-to-nitrogen bond in the out-of-plane direction for HBNF bilayer. Figure 2f clearly indicates the oppositely directed P_z for boron and nitrogen atoms for all stacking orders. Because of this, there is no possibility of e_{zyy} . The single boron–nitride monolayer decorated with hydrogen and fluorine yield significant e_{yyy} and e_{zyy} values.^[46] The present HBNF consists of three boron–nitrogen bonds (similar to diamane), which cancels the generated polarization under stretching. Such a cancellation was slightly avoided in case of HBNH and FBNF bilayers. The resultant e_{zyy} is six times smaller than that in HCF bilayers. The observations for e_{yyy} and e_{zyy} under tensile deformation further support the accuracy of derived potential parameters and simulation settings.

The vertical tensile deformation helps to determine the elastic coefficients (E^{zzzz} and $E^{\gamma yzz}$) and the piezoelectric coefficient e_{zzz} . We adopt the displacement control conditions to hold the top-most and bottom-most set of atoms. E^{zzzz} and $E^{\gamma yzz}$ for SMOs-a is 43.4 GPa (thickness as 9.35 Å) and from the previous report is 58 GPa.^[47] The observed difference (about 14 GPa) is mainly due to the removal of stress contributions from the holding atoms. Further, we perform only stretching simulations for three and four layered SMOs systems. Figure S3, Supporting Information, shows the out-of-plane elastic modulus variation with number of layers in SMOs. The resulting elastic coefficient E^{zzzz} was noted as 51.2 and 49.3 GPa, respectively. For four-layered SMOs, E^{zzzz} and $E^{\gamma yzz}$ are highly coinciding with the experimental bulk sample^[48] as well as DFT reported values^[49,50] for multi-layered systems. The e_{zzz} coefficient is 0.07 nC m⁻¹ for SeMoS-a to SeMoS-e (see Figure 2c). Whereas for multi-layer SeMoS system, e_{zzz} is noted as 0.43 nC m⁻¹.^[18] We extend our simulations for three and four layer SeMoS system with stacking order a and found the e_{zzz} as 0.22 and 0.36 nC m⁻¹, respectively. The observed values of e_{zzz} are also matching with the DFT predictions for multi-layers. This examines the results accuracy further. Other than bilayer HBNF ($e_{zzz} = 0.05$ nC m⁻¹), the remaining diamane bilayers show zero e_{zzz} values.

We now focus on the compressive loading simulations. As shown in Figure 1d, the subjection of left and right edge atoms along y-direction to an equal and opposite displacements (0.1 Å) lead to a natural bending deformation. The bilayer system is initially compressed, and buckling occurs at the critical compression strain. Later, with the increase of compressive strain, the deformation follows the shape at the critical strain, and there is no observation of other higher-order deformations. Supporting videos visualize the deformation of the bilayer system. First, we calculate the averaged curvature for the compressed system using Equation (S4), Supporting Information. The bending energy (E_b) is estimated as the difference of total energy per unit area between initial and current atomic states using Equation (S6), Supporting Information. Figure S6a, Supporting Information, indicates the response of E_b with square of curvature (κ^2). The bending stiffness D_b computed using Equation (S8), Supporting Information, for bilayer SMOs-a is 33.12 eV, which is in the experimental prediction range of 14–55 eV for aligned bilayers.^[51] For bilayer SeMoS-a, D_b is about 21.41 eV. Due to the force imbalance through the different chalcogen atom bonding on either side of the molybdenum atom, the bending deformation is achieved easily in SeMoS-a compared to SMOs-a. Similar observation made between FCF-a (142.73 eV) and HCF-a (114.57 eV).

Systems FBNF-a and FBNH-a show D_b as 105.51 and 86.77 eV, respectively. The diamane and BNdiamane show enhanced D_b compared to the TMDCs. The structural asymmetry in these layered systems helps to reduce the bending stiffness. Figure S4, Supporting Information, plots the bin averaged strain distribution along the compressive direction. The components ϵ_{yy} , ϵ_{zz} , and ϵ_{zy} are non-zero, and the remaining components are zero. From these non-zero strains, the total polarization P_z including piezoelectric and flexoelectric effects expressed as

$$P_z = e_{zyy}\epsilon_{yy} + e_{zzz}\epsilon_{zz} + \mu_{zyzy}\frac{\partial\epsilon_{zy}}{\partial y} + \mu_{zyzz}\frac{\partial\epsilon_{zz}}{\partial y} + \mu_{zyyy}\frac{\partial\epsilon_{yy}}{\partial y} \quad (1)$$

where $e_{\alpha\beta\gamma}$ and $\mu_{\alpha\beta\gamma\delta}$ represent the piezoelectric and flexoelectric coefficients. α , β , γ , and δ denote the Cartesian directions x , y , and z . The opposite variation of ϵ_{yy} and ϵ_{zz} (see Figure S4, Supporting Information) cancels the resultant piezoelectric part of polarizations $e_{zyy}\epsilon_{yy}$ and $e_{zzz}\epsilon_{zz}$. The associated average strain gradients for ϵ_{yy} and ϵ_{zz} are about 100 times smaller than the strain gradient $\frac{\partial\epsilon_{zy}}{\partial y}$. Also, the structural symmetry does not allow the coefficients μ_{zyyy} and μ_{zyzz} . Hence the only effective contribution is from ϵ_{zy} to the total polarization P_z . We calculate the average strain gradient $\epsilon_{zy,z}^a$ using Equation (S5), Supporting Information. Unlike earlier deformation prescribed reports,^[45,52] the strain gradient and curvature are not equal. Note that, the curvature uses the averaged coordinates and not depend on the atomic strain. The current scheme is free from prescribing the deformation pattern and the bending arise as a natural process.

Figure 4a shows the linear variation of P_z with $\epsilon_{zy,z}^a$ for SMOs, SeMoS, HCF, and FBNF bilayers in stacking order a. The flexoelectric coefficient μ_{zyzy} is 0.99 eC for SMOs-a, which is seven times higher than the monolayer SMOs^[45] (thickness of 6.5 Å is used to convert nC m⁻¹ units to eC units). A recent experimental study on thin SMOs film predicted the absolute value of flexoelectric coefficient as 0.23 nC m⁻¹.^[25] which is also seven times larger than the monolayer SMOs.^[45] DFT reports the flexoelectric coefficient value as 0.14,^[27] 0.004,^[28] and 0.032^[53] nC m⁻¹. The difference in these values is attributed to the consideration of different contributions to polarization, deformation scheme, thickness definition, etc. The original experimental investigation on monolayer SMOs reports the measured effective piezoelectric coefficient d_{zzz} about 1 to 1.5 pm V⁻¹^[22,23] and then converted into effective flexoelectric response under certain assumptions. In the current simulations, we have the recorded data of stress σ_{zz} during the compression process. Using that, we established a linear fitting across P_z and σ_{zz} , which yields the coefficient d_{zzz} as 2.58 pm V⁻¹ for SMOs-a. Figure S6b, Supporting Information, shows this variation for bilayer materials SMOs, SeMoS, HCF, and FBNF bilayers in stacking order a. For SMOs-e configuration, μ_{zyzy} is 0.42 eC and d_{zzz} is noted as 1.69 pm V⁻¹. Another recent experimental study^[54] reports d_{zzz} as 0.7–1.5 pm V⁻¹ (thickness is 4–90 nm) under same stacking as SMOs-e. This represent the enhancement of μ_{zyzy} over monolayer is strongly depending on the stacking order. Figure 4c shows μ_{zyzy} for SMOs-a to SMOs-e. The flexoelectric response in SMOs-b to SMOs-d similar to SMOs-e. Identical observations were made from the stacking orders in SeMoSe bilayer system.

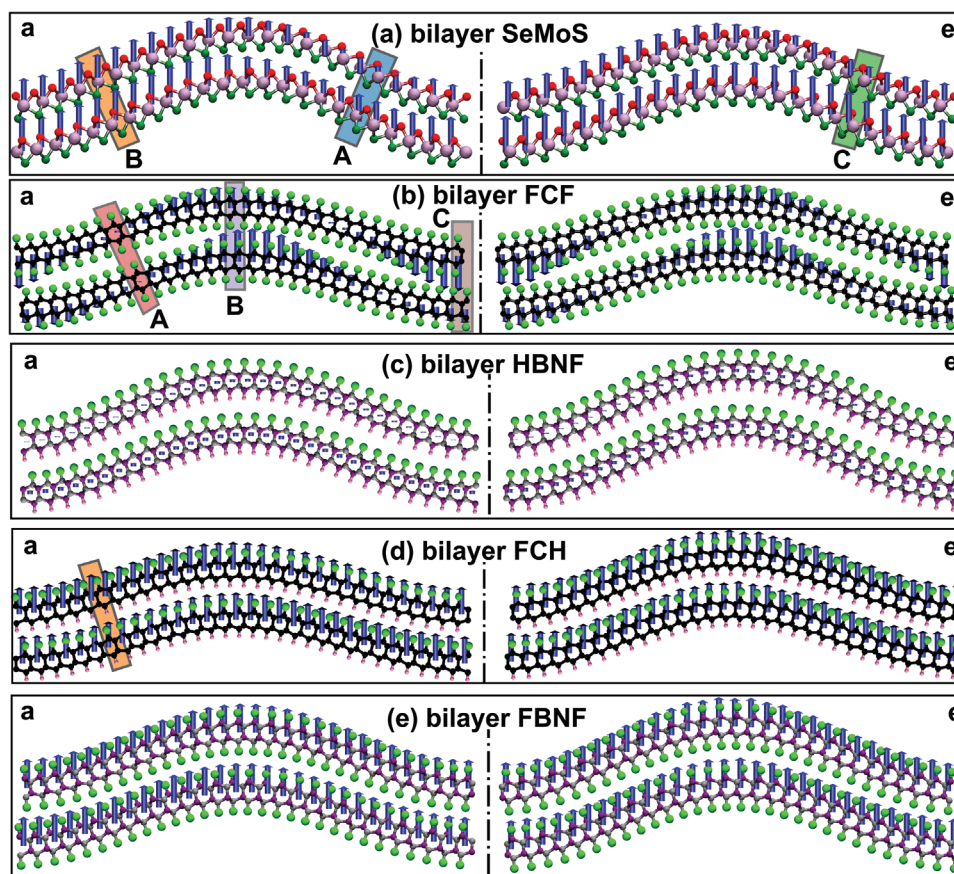


Figure 3. Deformed atomic configurations of bilayer a) SeMoS, b) FCH, c) FCF, d) HBNF, and e) FBNF in stacking order a (left side) and e (right side). Arrows indicate the bin averaged P_z . Data collected at same bending angle difference of 11.52° from initial state.

For SeMoS-a, μ_{zyz} is 0.93 eC, which is only 1.8 times than monolayer SeMoS (thickness 6.9 Å used to convert 0.117 nC m^{-1} ^[45] to 0.504 eC) and for SeMoS-e, μ_{zyz} is 1.98 eC. SeMoS-b, SeMoS-c, and SeMoS-d show higher μ_{zyz} compared to SeMoS-a (see Figure 4c). We note the coefficient d_{zzz} as 2.85 pm V^{-1} , and from DFT predictions for a multilayer SeMoS system is 2.58 pm V^{-1} ^[55] in stacking order e. An inverted trend is observed when compared to SMOs or SeMoSe bilayers. **Figure 3a** shows the polarization distribution along the compression direction for SeMoS-a and SeMoS-e. The polarization from atoms in the highlighted cells (A and C) is small in SeMoS-a and high in SeMoS-e. The bond angle variation at different strain gradients for cells A and B are plotted in Figure S7, Supporting Information. The bond angle for atoms in cell A is nearly constant and varies for cell B. Due to the no change in bond angle, the electron interactions (π - σ or σ - σ) are not effective to induce a dipole moment. As a result, the polarization corresponding to cell A is minimal. A lower scale of rigidity is observed for bond angle in cell C of SeMoS-e (Figure S7, Supporting Information), which help to raise the polarization. Also unlike SMOs, there exist interaction between sulfur and selenium from the bottom and top layers. That interaction also plays a significant role with respect to the stacking order in defining the polarization.

Figure 4a,b plots the P_z response for FCF-a and FCF-e. The generated P_z is very small in these systems. There is no

observation of linear variation of P_z for all stacking orders of FCF system. To confirm this observation, we plot the distribution of P_z over bins for each layer in Figure 3b. A cancellation of P_z is understood. The polarization for cell A is zero, and for cell B is maximum. The edge cell C shows a polarization that opposing the polarization in cell B. A similar trend is observed on the other side of Figure 3b. The fluorine atoms connected to carbon atoms result in an equal and opposite dipole moment p_z in cell A, which cancels the polarization P_z . In cell B, the bending induced change of bond length and bond angles creates an imbalance between carbon-fluorine bonds and results a p_z of 0.0034 eC\AA . Cell C is near to the loading edge creates an opposite strain response to cell B, which reverses the direction of p_z . Overall, the strong charge localization of fluorine atoms and the weak symmetry breakage avoid the changes in polarization for FCF. Similar observations were made for HCH system. To confirm the above observations, we repeated our calculations with monolayer FCF and HCH systems using the current scheme and obtained μ_{zyz} values that agree with earlier predictions.^[33] In a monolayer, the complete cancellation of P_z is avoided (as seen from bottom or top layer of Figure 3b). Whereas, in the bilayer system the response of P_z in each layer is in contrast with each other, which makes the P_z low and not linear.

The HBNF-a and HBNF-e configurations show very small P_z and there is no observation of linear relationship with the

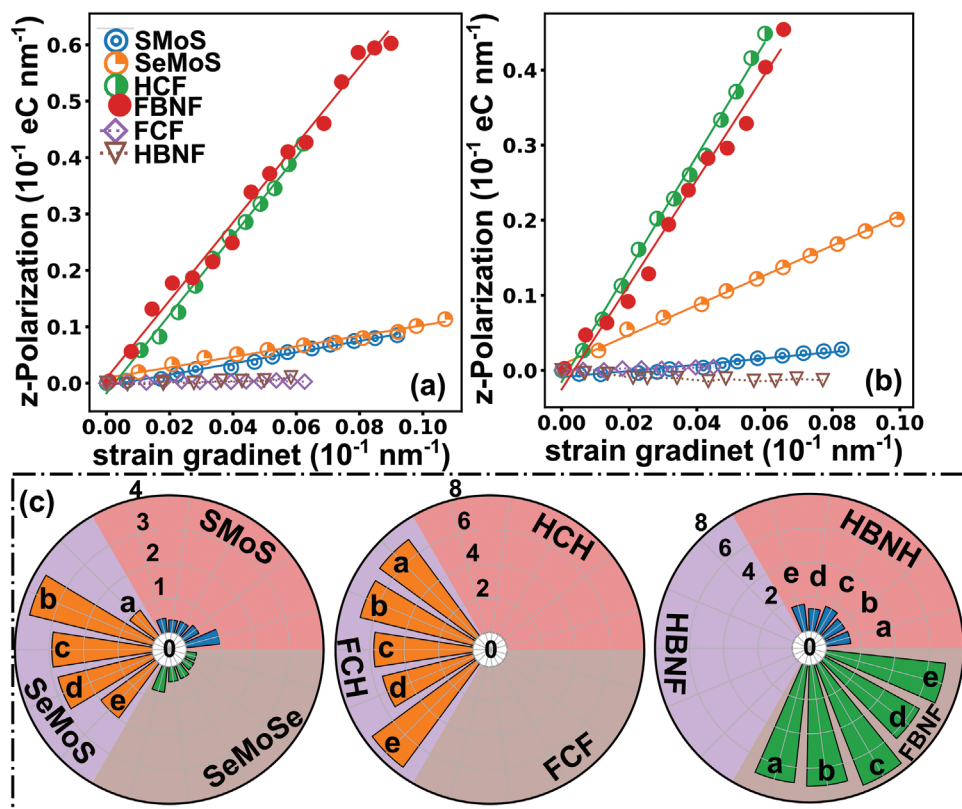


Figure 4. The response of polarization P_z with strain gradient $\varepsilon_{zy,z}^a$ for bilayer systems SMOs, SeMoS, HCF, FBNF, FCF, and HBNF with stacking order a) a and b) e. c) Flexoelectric coefficient (μ_{zyz}) values for all the considered materials in stacking orders a–e.

strain gradient (see Figure 4a,b). The atomic configurations in Figure 3c confirms the distribution of low P_z in stacking orders a and e. This is mainly due to the cancellation of dipole moments associated with each unitcell. The vertical dipole moment p_z is opposite for the bonds nitrogen–fluorine and boron–hydrogen. Out of the three central boron–nitrogen bonds, only the vertical bond maintain the dipole moment. The other two bonds align opposite to each other, and hence their dipole moments cancel with each other. The bending induced bond angle and bond length changes induce flexoelectric effect. However, the generated asymmetry in dipole moment is not overcoming the cancellation. As a total, the central bond is responsible for the total polarization in each layer. The P_z for HBNF-e is 0.00014 eC Å⁻¹ at bending angle 11.52°, which is ten times smaller than SeMoS-e at same bending angle. Other stacking orders b to d also perform in the similar manner and there is no observation of linear response. Hence μ_{zyz} values are noted as zero in Figure 4c.

The HCF materials outperform in generating the polarization under bending deformation. The μ_{zyz} for HCF-a is doubled with respect to bilayer TMDs (see Figure 4c). Unlike HBNF and FCF cases, here the cancellation of dipole moments avoided. As fluorine atoms gains more charge due to electron negativity character, the resultant dipole moment directed toward it. The total P_z for HCF-e is 0.0026 eC Å⁻¹, which is nearly twice that of SeMoS-e material at same bending angle 11.52°. This enhancement is similar in case of monolayer HCF^[33] and monolayer

SeMoS.^[45] For the selected unitcell in HCF-e in Figure 3d and SeMoS-e in Figure 3a at nearly same location and same bending angles, the percentage of change in bond length (bond angle) is 0.16 (2.35) and 0.45 (0.97), respectively. The higher changes in atomic configuration lead to higher local electric fields and high dipole moments. The change in bond angle is about 1.4 times higher than that observed in monolayer HCF, which strongly support the enhanced flexoelectric coefficient through the bonding or valence electron interactions. Other stacking orders a to d also show similar enhancement with allowed changes due to the different stacking order.

The non-Janus FBNF interestingly showing high polarization values. In this case, the hydrogen atom in HBNF changed to fluorine atom. Because of the boron–fluorine bond, the dipole moment strengthens and reversed the direction toward fluorine atom. Figure 3e shows the unidirectional p_z for all bins in stacking order a and e. The fluorine atom collects more charge from the boron atom compared to the collection by the nitrogen atom. The total dipole moment in the lower layer central cell for this bond is 0.44 eCÅ, and for other bonds is –0.18 eCÅ, which makes a non-zero contribution to the total polarization P_z . Figure 4a,b shows the linear variation for P_z with strain gradient for FBNF-a and FBNF-e. The noted coefficient μ_{zyz} is similar to the HCF-e. The electron interaction strengths may differ in stacking orders b to d for FBNF causing a rise in μ_{zyz} compared to HCF-b to HCF-d (see Figure 4c). For the non-Janus HBNH, the μ_{zyz} is in the order of bilayer Janus TMDs. In

HBNH, the hydrogen–boron bond gains more dipole moment than the rest of the bonds, similar to the FBNF case. However, due to low electron negativity character for hydrogen, the induced dipole moment is weaker than boron–fluorine bond. As a result, μ_{zyz} is reduced. An identical variation between stacking orders is observed for both FBNF and HBNH.

3. Conclusion

In summary, we propose an innovative and accurate computational approach on the basis of DFT and MLIPs with incorporated long-range vdW and electrostatic interactions to explore the flexoelectric response of 2D vdW bilayers. The short-range interactions are accurately defined using the MLIPs trained over computationally inexpensive DFT datasets and long-range interaction parameters are calibrated from DFT simulations. The in-plane and out-of-plane tensile loading conducted using the most popular platform for the standard MD simulations, enabled us to test the accuracy of the devised modeling strategy. The predicted mechanical properties by the proposed computationally efficient method show an excellent level of agreement with those by the plane-wave DFT. After ensuring the outstanding accuracy of our developed technique, we further explored the effects of stacking orders (a–e) in bilayer TMDs, diamanes, and BNdiamanes. Our predicted piezoelectric coefficients for TMDs agree with the earlier experimental and full-DFT reports. The natural bending process is then simulated via the edge compression, from which, curvature, strain gradient, stress, and polarization are quantified. Bilayer TMDs are found to be about four times softer than diamanes. The effective piezoelectric coefficient predicted in this work matches excellently with earlier experiments. TMDs bending flexoelectric coefficient is predicted to be 2–7 times higher than that of the monolayer counterpart, depending on the stacking orders. Bilayer Janus diamane (HCF) outperforms TMDs, with the enhancement of 20 times. The non-Janus diamanes (FCF and HCH) cancel the change in polarization due to bending and the flexoelectric effect is diminished. The Janus bilayer HBNF system also cancels the polarization due to the dipole moment reversal across the boron–hydrogen and nitrogen–fluorine bonds. The non-Janus FBNF diamane performs similarly to HCF, whereas HBNH yields a low enhancement due to the lower electron interactions. The presented methodology of deriving potential parameters is easily extendable to handle grain boundaries, Moiré patterns, lattice-mismatched bilayer supercells, and to perform complex deformation conditions. Obtained flexoelectricity results can enhance the design of next-generation energy harvesters. The proposed MLIP-based methodology is moreover believed to offer a robust tool to simulate the complex flexoelectric response of novel vdW heterostructures and can be also extended for other cutting-edge applications.

4. Computational Methods

In DFT calculations, periodic boundary conditions were applied along all three Cartesian directions. The unitcell size in bilayer normal direction (z) was set to 50 Å, to avoid interactions with

periodic replicas. Such unitcells undergo geometric optimization using conjugate-gradient method with a convergence criterion of 0.001 eV Å⁻¹ for Hellmann–Feynman forces with 15 × 15 × 1 k -point mesh. The generalized gradient approximation and Perdew–Burke–Ernzerhof functional were considered with an energy cutoff of 500 eV for the plane waves and a convergence criterion of 10⁻⁵ eV for the electronic self-consistent-loop. The AIMD runs performed under Nosé thermostat with time step 1 fs using 2 × 2 × 1 k -point grid.

We perform both in-plane and out-of-plane stretching deformations to study the mechanical and piezoelectric properties of bilayer atomic system size 8 × 8 nm². Such simulations serve as a benchmark tests for the derived inter-atomic potential parameters. For in-plane stretching deformation, we supply same displacement of 0.0005 Å to the atoms in right edge and -0.0005 Å to the atoms in left edge. In out-of-plane stretching case, supplied similar displacement to the top and bottom most atom sets. The stretching simulations performed until the strain reaches to 0.01.

To achieve the bending deformation, we consider compressing the left and right edge atoms. Figure 1d shows the schematic setup for compression. Here, we supply displacement higher than the stretching case (0.1 Å). This helps to increase the atomic forces and lead to bending deformation. In tensile and compressive conditions of loading, we supply the displacement only for ten time steps and relax for 10 000 time steps. Out-of-these relaxation steps, the data is collected for every 1000 steps. Before applying the loading conditions, atomic systems are equilibrated using Nosé–Hoover thermostat under velocity Verlet integration scheme with time increment of 0.5 fs. During the relaxation, the edge atoms are held fixed. We use Large-scale Atomic/Molecular Massively Parallel Simulator (LAMMPS)^[56] to perform the MD simulations. Vienna Ab-initio Simulation Package (VASP)^[57–59] employed in creating training sets and estimating the inter-layer energy.

Supporting Information

Supporting Information is available from the Wiley Online Library or from the author.

Acknowledgements

The authors gratefully acknowledge the sponsorship from the ERC Starting Grant COTOFLEXI (Grant No. 802205). The authors also acknowledge the support of the cluster system team at the Leibniz Universität of Hannover, Germany. The authors would like to thank Prof. Alexander Shapeev for his discussions and support to this work.

Open access funding enabled and organized by Projekt DEAL.

Conflict of Interest

The authors declare no conflict of interest.

Data Availability Statement

The data that support the findings of this study are available from the corresponding author upon reasonable request.

Keywords

bending deformation, charge-dipole model, flexoelectricity, machine learning, van der Waals bilayers

Received: April 21, 2022

Revised: May 15, 2022

Published online: July 21, 2022

- [1] W. Ma, L. E. Cross, *Appl. Phys. Lett.* **2006**, *88*, 232902.
- [2] R. Mbarki, J. B. Haskins, A. Kinaci, T. Cagin, *Phys. Lett. A* **2014**, *378*, 2181.
- [3] S. S. Nanthakumar, X. Zhuang, H. S. Park, T. Rabczuk, *J. Mech. Phys. Solids* **2017**, *105*, 217.
- [4] B. He, B. Javvaji, X. Zhuang, *Phys. B* **2018**, *545*, 527.
- [5] T. D. Nguyen, S. Mao, Y. W. Yeh, P. K. Purohit, M. C. McAlpine, *Adv. Mater.* **2013**, *25*, 946.
- [6] F. Ahmadpoor, P. Sharma, *Nanoscale* **2015**, *7*, 16555.
- [7] F. Vasquez-Sancho, A. Abdollahi, D. Damjanovic, G. Catalan, *Adv. Mater.* **2018**, *30*, 1705316.
- [8] C. Stefani, E. Langenberg, K. Cordero-Edwards, D. G. Schlom, G. Catalan, N. Domingo, *J. Appl. Phys.* **2021**, *130*, 074103.
- [9] J.-H. Liu, X. Chen, Y. Li, X. Guo, H.-X. Ge, Q.-D. Shen, *Appl. Phys. Lett.* **2018**, *113*, 042903.
- [10] K. S. Moreira, E. Lorenzett, A. L. Devens, Y. A. Santosda Campo, D. Mehler, T. A. L. Burgo, *J. Appl. Phys.* **2021**, *129*, 234502.
- [11] L. Sun, L. Zhu, C. Zhang, W. Chen, Z. Wang, *Nano Energy* **2021**, *83*, 105855.
- [12] S. J. Liang, B. Cheng, X. Cui, F. Miao, *Adv. Mater.* **2020**, *32*, 1903800.
- [13] C. Li, P. Zhou, D. W. Zhang, *J. Semicond.* **2017**, *38*, 3.
- [14] J. He, C. Wang, B. Zhou, Y. Zhao, L. Tao, H. Zhang, *Mater. Horiz.* **2020**, *7*, 2903.
- [15] D. Lin, S. Li, J. Wen, H. Berger, L. Forró, H. Zhou, S. Jia, T. Taniguchi, K. Watanabe, X. Xi, M. S. Bahrmy, *Nat. Commun.* **2020**, *11*, 2406.
- [16] S. Lei, J. Lin, Y. Jia, M. Gray, A. Topp, G. Farahi, S. Klemenz, T. Gao, F. Rodolakis, J. L. McChesney, C. R. Ast, A. Yazdani, K. S. Burch, S. Wu, N. P. Ong, L. M. Schoop, *Sci. Adv.* **2020**, *6*, eaay6407.
- [17] X. Wang, X. Zhou, A. Cui, M. Deng, X. Xu, L. Xu, Y. Ye, K. Jjiang, L. Shang, L. Zhu, J. Zhang, Y. Li, Z. Hu, J. Chu, *Mater. Horiz.* **2021**, *8*, 1985.
- [18] L. Dong, J. Lou, V. B. Shenoy, *ACS Nano* **2017**, *11*, 8242.
- [19] H. Cai, Y. Guo, H. Gao, W. Guo, *Nano Energy* **2019**, *56*, 33.
- [20] Y. Li, X. Wang, D. Tang, X. Wang, K. Watanabe, T. Taniguchi, D. R. Gamelin, D. H. Cobden, M. Yankowitz, X. Xu, J. Li, *Adv. Mater.* **2021**, *33*, 2105879.
- [21] J. Dong, B. Cai, G. Ouyang, *J. Phys. Chem. C* **2021**, *125*, 11318.
- [22] C. J. Brennan, R. Ghosh, K. Koul, S. K. Banerjee, N. Lu, E. T. Yu, *Nano Lett.* **2017**, *17*, 5464.
- [23] C. J. Brennan, K. Koul, N. Lu, E. T. Yu, *Appl. Phys. Lett.* **2020**, *116*, 053101.
- [24] M. Wu, X. Zhang, X. Li, K. Qu, Y. Sun, B. Han, R. Zhu, X. Gao, J. Zhang, K. Liu, X. Bai, X. Z. Li, P. Gao, *Nat. Commun.* **2022**, *13*, 216.
- [25] H. Hirakata, Y. Fukuda, T. Shimada, *J. Phys. D: Appl. Phys.* **2022**, *55*, 125302.
- [26] T. Dumitrică, C. M. Landis, B. I. Yakobson, *Chem. Phys. Lett.* **2002**, *360*, 182.
- [27] S. Kumar, D. Codony, I. Arias, P. Suryanarayana, *Nanoscale* **2021**, *13*, 1600.
- [28] M. Springolo, M. Royo, M. Stengel, *Phys. Rev. Lett.* **2021**, *127*, 216801.
- [29] W. Shi, Y. Guo, Z. Zhang, W. Guo, *J. Phys. Chem. Lett.* **2018**, *9*, 6841.
- [30] A. N. Morozovska, E. A. Eliseev, H. V. Shevliakova, Y. Y. Lopatina, G. I. Dovbeshko, M. D. Glinchuk, Y. Kim, S. V. Kalinin, *Phys. Rev. Appl.* **2021**, *15*, 044051.
- [31] A. G. Kvashnin, P. B. Sorokin, B. I. Yakobson, *J. Phys. Chem. Lett.* **2015**, *6*, 2740.
- [32] D. G. Kvashnin, A. T. Matveev, O. I. Lebedev, B. I. Yakobson, D. Golberg, P. B. Sorokin, D. V. Shtansky, *J. Phys. Chem. Lett.* **2018**, *9*, 5086.
- [33] B. Javvaji, B. Mortazavi, X. Zhuang, T. Rabczuk, *Carbon* **2021**, *185*, 558.
- [34] I. S. Novikov, K. Gubaev, E. Podryabinkin, A. V. Shapeev, *Mach. Learn.: Sci. Technol.* **2021**, *2*, 025002.
- [35] B. Mortazavi, F. Shojaei, B. Javvaji, M. Azizi, H. Zhan, T. Rabczuk, X. Zhuang, *Appl. Surf. Sci.* **2020**, *528*, 147035.
- [36] B. Mortazavi, E. V. Podryabinkin, I. S. Novikov, T. Rabczuk, X. Zhuang, A. V. Shapeev, *Comput. Phys. Commun.* **2021**, *258*, 107583.
- [37] B. Mortazavi, I. S. Novikov, E. V. Podryabinkin, S. Roche, T. Rabczuk, A. V. Shapeev, X. Zhuang, *Appl. Mater. Today* **2020**, *20*, 100685.
- [38] S. Grimme, J. Antony, S. Ehrlich, H. Krieg, *J. Chem. Phys.* **2010**, *132*, 154104.
- [39] S. Grimme, S. Ehrlich, L. Goerigk, *J. Comput. Chem.* **2011**, *32*, 1456.
- [40] M. J. Frisch, G. W. Trucks, H. B. Schlegel, G. E. Scuseria, M. A. Robb, J. R. Cheeseman, G. Scalmani, V. Barone, G. A. Petersson, H. Nakatsuji, X. Li, M. Caricato, A. V. Marenich, J. Bloino, B. G. Janesko, R. Gomperts, B. Mennucci, H. P. Hratchian, J. V. Ortiz, A. F. Izmaylov, J. L. Sonnenberg, D. Williams-Young, F. Ding, F. Lipparini, F. Egidi, J. Goings, B. Peng, A. Petrone, T. Henderson, D. Ranasinghe, et al., *Gaussian 16 Revision B.01*, Gaussian Inc., Wallingford, CT **2016**.
- [41] X. Zhuang, B. He, B. Javvaji, H. S. Park, *Phys. Rev. B* **2019**, *99*, 054105.
- [42] B. Javvaji, B. He, X. Zhuang, *Nanotechnology* **2018**, *29*, 225702.
- [43] M. H. Naik, I. Maity, P. K. Maiti, M. Jain, *J. Phys. Chem. C* **2019**, *123*, 9770.
- [44] S. Wei, J. Li, X. Liao, H. Jin, Y. Wei, *J. Phys. Chem. C* **2019**, *123*, 22570.
- [45] B. Javvaji, B. He, X. Zhuang, H. S. Park, *Phys. Rev. Mater.* **2019**, *3*, 125402.
- [46] M. Noor-A-alam, H. J. Kim, Y. H. Shin, *Phys. Chem. Chem. Phys.* **2014**, *16*, 6575.
- [47] J. U. Lee, S. Woo, J. Park, H. C. Park, Y. W. Son, H. Cheong, *Nat. Commun.* **2017**, *8*, 1370.
- [48] J. L. Feldman, *J. Phys. Chem. Solids* **1976**, *37*, 1141.
- [49] H. Peelaers, C. G. Van de Walle, *J. Phys. Chem. C* **2014**, *118*, 12073.
- [50] H. Eidsvåg, M. Rasukkannu, D. Velauthapillai, P. Vajeeston, *RSC Adv.* **2021**, *11*, 3759.
- [51] J. Yu, E. Han, M. A. Hossain, K. Watanabe, T. Taniguchi, E. Ertekin, A. M. van der Zande, P. Y. Huang, *Adv. Mater.* **2021**, *33*, e2007269.
- [52] T. Pandey, L. Covaci, F. Peeters, *Carbon* **2021**, *171*, 551.
- [53] J. Dong, H. Hu, H. Li, G. Ouyang, *Phys. Chem. Chem. Phys.* **2021**, *23*, 20574.
- [54] H. Hallil, W. Cai, K. Zhang, P. Yu, S. Liu, R. Xu, C. Zhu, Q. Xiong, Z. Liu, Q. Zhang, *Adv. Electron. Mater.* **2022**, *2101131*, <https://doi.org/10.1002/aelm.202101131>.
- [55] T. H. Pham, H. Ullah, A. Shafique, H. J. Kim, Y.-H. Shin, *Phys. Chem. Chem. Phys.* **2021**, *23*, 16289.
- [56] S. Plimpton, *J. Computat. Physics* **1995**, *117*, 1.
- [57] G. Kresse, D. Joubert, *Phys. Rev. B* **1999**, *59*, 1758.
- [58] G. Kresse, J. Furthmüller, *Phys. Rev. B* **1996**, *54*, 11169.
- [59] G. Kresse, J. Furthmüller, *Comput. Mater. Sci.* **1996**, *6*, 15.